Entanglement in shape phase transitions of coupled molecular benders

M. Calixto*
Departamento de Matemática Aplicada, Facultad de Ciencias, Universidad de Granada, Campus de Fuentenueva s/n, 18071 Granada, Spain

F. Pérez-Bernal†
Departamento de Física Aplicada, Unidad Asociada IEM-CSIC, Facultad de Ciencias Experimentales, Universidad de Huelva, Campus del Carmen, Avenida de las Fuerzas Armadas s/n, 21071 Huelva, Spain

(Received 25 December 2013; published 24 March 2014)

We study the entanglement properties of the shape phase transitions between different geometric limits of two coupled equivalent molecular benders modeled with the two-dimensional limit of the vibron model. This system has four possible geometric configurations: linear, *cis*-bent, *trans*-bent, and nonplanar. We show how the entanglement, accessed through the calculation of the linear entropy, between benders and between rotational and vibrational degrees of freedom changes sensitively in the critical regions of this two-fluid bosonic model. The numeric calculation is complemented with a variational approach to the ground-state wave function in terms of symmetry-adapted coherent states.

DOI: 10.1103/PhysRevA.89.032126 PACS number(s): 03.65.Fd, 33.20.Vq, 05.30.Rt, 03.65.Ud

I. INTRODUCTION

A correct understanding and description of entanglement are a fundamental aim of quantum information science. The occurrence of entanglement implies inherently quantum correlations in the system. An appropriate description of these correlations is of great relevance in fields such as quantum computing, quantum teleportation, and quantum cryptography.

In recent times, the study of entanglement in quantum many-body systems and its relation to quantum phase transitions (QPTs) and quantum chaos has acquired great momentum. The complex correlations and collective behavior that take place in critical systems have attracted a huge degree of attention, but a complete theory of many-body entanglement is still missing.

Large correlations and collective behavior are an intrinsic part of critical systems, and therefore entanglement measures should capture the essence of QPTs. In this respect, the entanglement properties of a single-mode Dicke model [1,2], a two-mode Bose-Einstein condensate [3], and the vibration-rotation entanglement in the two-dimensional limit of the vibron model [4] can be found in the literature.

We are interested in an extension of the latter case. The vibron model was originally introduced by Iachello in the 1980s [5,6] to study rotational and vibrational spectra in diatomic molecules. Like other similar algebraic approaches, e.g., the interacting boson model [7], this model is based on the concept of spectrum-generating algebra (SGA). The vibron model was later extended to the study of polyatomic molecules, and its one- and two-dimensional (2DVM) limits were introduced for the study of pure vibrations and bending dynamics, respectively.

The 2DVM, based on a U(3) SGA, describes a planar system containing a dipole degree of freedom [8]. It is an appropriate model for the study of critical properties because it is the simplest two-level model which still retains a nontrivial angular momentum quantum number. The basic physical realization of such a system is the bending vibrational mode of a molecule [9,10]. In the 2DVM one finds different phases connected to specific geometric configurations of the ground state and related to distinct dynamic symmetries of the Hamiltonian [11] like other algebraic models of nuclear and molecular structure. The 2DVM, despite its simplicity, embodies the necessary physical ingredients to reproduce the spectroscopic signatures of its limiting cases, the rigidly linear and rigidly bent configurations, as well as the interesting situations in between these two cases [12,13].

QPTs in algebraic models, also called ground-state phase transition in the seminal works of Gilmore [14], occur when qualitative changes of the system's ground state take place for small changes of a Hamiltonian control parameter ξ in the vicinity of a critical value of the parameter. The Hamiltonian is written as a convex combination $H(\xi) = (1-\xi)H_1 + \xi H_2$. At $\xi = 0$ the system is in phase I, characterized by the dynamical symmetry G_1 of H_1, and at $\xi = 1$ the system is in phase II, characterized by the dynamical symmetry G_2 of H_2 [11]. Recent reviews on quantum phase transitions in algebraic models can be found in Refs. [15–17].

The coupling of two U(3) SGAs extends the 2DVM model to encompass coupled benders [8,18,19]. Because this is a two-fluid bosonic model, the number of available dynamical symmetries and limiting geometrical configurations is much larger in the coupled 2DVM than in the single-bender model. Therefore the ground-state phase diagram in the coupled U(3) case is more complex than in the single-bender case [20,21]. This was previously observed in the study of the phase diagram of IBM-2 (interacting boson model version 2), another two-fluid bosonic model in the realm of nuclear physics where a distinction is made between protons and neutrons [22–24].

The coupled 2DVM has been applied to molecular structure problems to reproduce the bending vibrational spectra of molecules with coupled benders. The model was originally used to reproduce the bending vibrational spectrum of the ground electronic state of acetylene (C_2H_2, $\tilde{X}\ ^1\Sigma_g^+$) [8,19,25], was later applied to a nonplanar molecule (ground electronic state of water peroxide, H_2O_2) [26], and has recently been extended to the vibrational bending spectroscopy of nonlinear planar species in *cis* and *trans* configurations [27]. Extensive

*calixto@ugr.es
†francisco.perez@dfaie.uhu.es

work on the bending dynamics of tetratomic molecules using other alternative approaches can be found in the literature [28–32]. In the shape-phase-transition case, works based on normal-mode bifurcations are of particular relevance [33,34].

The classical, thermodynamic, or mean-field limit of the different quantum (shape) phases of the vibron model is investigated by using an algorithm introduced by Gilmore [14] which makes use of semiclassical (boson-condensate) coherent states (CSs; see, e.g., [35–38] for standard references on CSs and [39] for a recent review on entangled coherent states) as variational states to approximate the ground-state energy. This approach was extended in Refs. [40–42] to nuclear systems and in Refs. [43–45] to molecular systems.

However, these trial states do not have a definite parity, and thus they do not display the intrinsic parity symmetry (see, e.g., [46]) present in the Hamiltonian. The key role of parity has recently been noticed in the context of QPT from normal to superradiant configurations in the Dicke model for matter-field (spin-boson) interactions [47,48] and in the QPT between linear and bent configurations of a single bender [4]. We extend this study to the case of coupled benders and, as anticipated in the single-bender case, we shall see that disregarding parity leads to an absence of entanglement for the usual variational approximations to the ground state in terms of (non-symmetry-adapted) CSs. To overcome this difficulty we introduce even (odd) CSs adapted to the parity symmetry of the Hamiltonian to better describe the ground (first excited) state of our model. These even and odd CSs are *Schrödinger-cat–like states* in the sense that they are a quantum superposition of quasiclassical, macroscopically distinguishable (having a negligible overlap) states. We shall show that even-cat states provide finite-size N approximations to some $N=\infty$ quantities like the ground-state energy "per particle" and order parameters like the *equilibrium radius*. The finite-size corrections obtained with these trial states differ from a systematic expansion of the different observables as a function of system's size, computing the relevant corrections for each power of N [49]. However, the main advantage of including even-cat states as a variational ansatz is that they offer the possibility of capturing, qualitatively and quantitatively, entanglement measures of the exact ground state for finite N values.

The outline of this article is as follows. After these introductory remarks, Sec. II revisits the coupled 2DVM and its semiclassical analysis based on CSs. Section III introduces the new, symmetry-adapted, even cat states for the coupled 2DVM and the results of the variational analysis using these new states compared to the results in the previous section. Section IV presents the different entanglement schemes considered and the results of exact (numeric) calculations compared with the results of traditional and symmetry-adapted semiclassical approaches. Finally, some concluding remarks are given in Sec. V.

II. MODEL HAMILTONIAN AND SEMICLASSICAL ANALYSIS

We briefly review the theoretical framework of the coupled 2DVM; the interested reader can find more details in Refs. [8,19,27]. The bosonic $U_1(3)\times U_2(3)$ algebra for coupled 2D systems can be constructed with the bilinear products of boson creation and annihilation operators. The Cartesian τ-boson operators $\{\tau^\dagger_{x,j},\tau^\dagger_{y,j},\tau_{x,j},\tau_{y,j}\}$ and a scalar σ boson $\{\sigma^\dagger_j,\sigma_j\}$ are the basic building blocks for the SGA, where the subscript $j=1,2$ denotes the subsystem. It is convenient to introduce circular bosons: $\tau_{\pm,j}=\mp(\tau_{x,j}\mp i\tau_{y,j})/\sqrt{2}$. The nine generators of each $U_j(3)$ algebra are the possible bilinear products of creation and annihilation operators with index j. In particular,

$$\begin{aligned}
\hat{n}_j &= \tau^\dagger_{+,j}\tau_{+,j}+\tau^\dagger_{-,j}\tau_{-,j},\\
\hat{n}_{\sigma,j} &= \sigma^\dagger_j\sigma_j,\\
\hat{\ell}_j &= \tau^\dagger_{+,j}\tau_{+,j}-\tau^\dagger_{-,j}\tau_{-,j},\\
\hat{D}_{+,j} &= \sqrt{2}(\tau^\dagger_{+,j}\sigma_j-\sigma^\dagger_j\tau_{-,j}),\\
\hat{D}_{-,j} &= \sqrt{2}(-\tau^\dagger_{-,j}\sigma_j+\sigma^\dagger_j\tau_{+,j}),\\
\hat{Q}_{+,j} &= \sqrt{2}\tau^\dagger_{+,j}\tau_{-,j},\\
\hat{Q}_{-,j} &= \sqrt{2}\tau^\dagger_{-,j}\tau_{+,j}
\end{aligned}\tag{1}$$

denote the number operators of vector ($\hat{n}_j$) and scalar ($\hat{n}_{\sigma,j}$) bosons, the 2D angular momentum $\hat{\ell}_j$, the dipole operator $\hat{D}_{\pm,j}$, and the quadrupole operator $\hat{Q}_{\pm,j}$ of $j=1,2$ type (see Ref. [11] for a discussion of the role of the $\hat{R}_{\pm,j}$ generators, which will not be used in the present work).

The total number of bosons, $\hat{N}=\sum_{j=1}^2\hat{N}_j$, with $\hat{N}_j=\hat{n}_j+\hat{n}_{\sigma,j}$, and the total 2D angular momentum, $\hat{\ell}_{12}=\sum_{j=1}^2\hat{\ell}_j$, are conserved quantities in the model. Moreover, we consider henceforth indistinguishable benders (e.g., $ABBA$-type molecules), so that $N_1=N_2=N/2$. We shall deal with four dynamical symmetry limits [see Eq. (1) in Ref. [21]] in the same spirit as previous works on the phase diagram for two-fluid bosonic systems [22–24]. To capture the essentials of the phase transition it is enough to consider a model Hamiltonian given by the following convex combination [21]:

$$\begin{aligned}
\hat{H} = \varepsilon\Bigg\{&(1-\xi)\left[\hat{n}_1+\hat{n}_2+\frac{\eta_1}{N}\hat{Q}_1\cdot\hat{Q}_2\right]\\
&+\xi\left[\frac{\hat{P}_1+\hat{P}_2}{N-2}+2\eta_2\frac{\hat{W}_1\cdot\hat{W}_2}{N}\right]\Bigg\},
\end{aligned}\tag{2}$$

where $\hat{P}_j=N_j(N_j+1)-\hat{W}_j^2$ is the $SO_j(3)$ pairing operator. The operator $\hat{W}_j^2=(\hat{D}_{+,j}\hat{D}_{-,j}+\hat{D}_{-,j}\hat{D}_{+,j})/2+\hat{\ell}_j^2$ is the $SO_j(3)$ second-order Casimir operator, and

$$\begin{aligned}
\hat{W}_1\hat{W}_2 &= (\hat{D}_{+,1}\hat{D}_{-,2}+\hat{D}_{-,1}\hat{D}_{+,2})/2+\hat{\ell}_1\hat{\ell}_2,\\
\hat{Q}_1\hat{Q}_2 &= \hat{Q}_{+,1}\hat{Q}_{-,2}+\hat{Q}_{-,1}\hat{Q}_{+,2},
\end{aligned}\tag{3}$$

are linked with the $SO_{12}(3)$ and $U_{12}(2)$ second-order Casimir operators, respectively. The parameter ε is an overall energy scale, whereas ξ,η_1, and η_2 are control parameters, whose values determine the system's geometry and its placement in the phase diagram.

The quantum number N_j determines the total number of bound states for the jth bender and labels the totally symmetric $[(N_j+1)(N_j+2)/2]$-dimensional representation $[N_j]$ of $U_j(3)$. For the direct product $U_1(3)\times U_2(3)$, the Hilbert space is spanned by the orthonormal basis vectors (in compact spectroscopic notation, removing N_j labels for the

sake of brevity):

$$|n_1^{\ell_1};n_2^{\ell_2}\rangle = \prod_{j=1}^{2} \frac{(\sigma_j^\dagger)^{N_j-n_j}(\tau_{+,j}^\dagger)^{\frac{n_j+\ell_j}{2}}(\tau_{-,j}^\dagger)^{\frac{n_j-\ell_j}{2}}}{\sqrt{(N_j-n_j)!\left(\frac{n_j+\ell_j}{2}\right)!\left(\frac{n_j-\ell_j}{2}\right)!}}|0\rangle, \quad (4)$$

where the bending quantum number $n_j = 0,1,\ldots,N_j$ and the angular momentum $\ell_j = n_j - 2m_j$ ($m_j = 0,1,\ldots,n_j$) are the eigenvalues of $\hat{n}_j$ and $\hat{\ell}_j$, respectively. We recall that we are considering the particular case $N_1 = N_2 = N/2$, so that the dimension of our Hilbert space is $[(N+2)(N+4)/8]^2$.

The matrix elements of the Hamiltonian (2) in the basis (4) can easily be derived. We direct the reader to Ref. [19] for an explicit expression of the matrix elements of each operator in $\hat{H}$, and here we shall just point out that whereas $\hat{n}_j$ and $\hat{Q}_1\hat{Q}_2$ preserve the so-called polyad number $\hat{n} \equiv \hat{n}_1 + \hat{n}_2$, the operators $\hat{P}_j$ and $\hat{W}_1\hat{W}_2$ do not conserve the polyad number $\hat{n}$; however, they still preserve parity $\hat{\Pi} \equiv e^{i\pi\hat{n}}$. Indeed, one can prove that $[\hat{H},\hat{\Pi}] = 0$, and both operators can then be jointly diagonalized. We shall come back to this point in Sec. III.

We now briefly discuss the classical limit of the coupled 2DVM using the coherent-state formalism (see Refs. [21,27] for more details). The connection between the abstract algebraic description and the conventional potential description is made through the CS:

$$\begin{aligned} |r_1,\theta_1;r_2,\theta_2\rangle &\equiv \frac{1}{\sqrt{N_1!N_2!}}(b_1^\dagger)^{N_1}(b_2^\dagger)^{N_2}|0\rangle, \\ b_j^\dagger &\equiv \frac{1}{\sqrt{1+r_j^2}}(\sigma_j^\dagger + r_j\cos\theta_j\tau_{x,j}^\dagger + r_j\sin\theta_j\tau_{y,j}^\dagger), \end{aligned} \quad (5)$$

with $r_1,r_2 \in \mathbb{R}$ and $\theta_1,\theta_2 \in [0,\pi)$ being free variational parameters. For future use, we shall provide the expression of the coefficients of the expansion of (5) in terms of the basis vectors (4), which is explicitly given by

$$\begin{aligned} &|r_1,\theta_1;r_2,\theta_2\rangle \\ &= \sum_{n_1,n_2=0}^{N_1,N_2}\sum_{m_1,m_2=0}^{n_1,n_2} c_{n_1,m_1}^{(N_1)}(r_1,\theta_1)c_{n_2,m_2}^{(N_2)}(r_2,\theta_2)\left|n_1^{n_1-2m_1};n_2^{n_2-2m_2}\right\rangle, \\ &c_{n_j,m_j}^{(N_j)}(r_j,\theta_j) \\ &= \sqrt{\binom{N_j}{n_j}\binom{n_j}{m_j}}\frac{(-r_j/\sqrt{2})^{n_j}(-1)^{m_j}e^{-i(n_j-2m_j)\theta_j}}{\left(1+r_j^2\right)^{N_j/2}}. \end{aligned} \quad (6)$$

The variational parameters r_j,θ_j are fixed by minimizing the mean energy per particle [21]:

$$\begin{aligned} &\mathcal{E}_{\xi,\eta_{1,2}}(r_{1,2},\phi) \\ &= \frac{\langle r_1,\theta_1;r_2,\theta_2|\hat{H}|r_1,\theta_1;r_2,\theta_2\rangle}{\varepsilon N} \\ &= (1-\xi)\left[\frac{1}{2}\sum_{j=1}^{2}\frac{r_j^2}{1+r_j^2} + \frac{\eta_1\cos(2\phi)}{4}\prod_{j=1}^{2}\frac{r_j^2}{1+r_j^2}\right] \\ &\quad + \xi\left[\frac{1}{4}\sum_{j=1}^{2}\left(\frac{1-r_j^2}{1+r_j^2}\right)^2 + 2\eta_2\cos(\phi)\prod_{j=1}^{2}\frac{r_j}{1+r_j^2}\right], \end{aligned} \quad (7)$$

which only depends on the dihedral angle $\phi = \theta_1 - \theta_2$. Note that $\mathcal{E}_{\xi,\eta_{1,2}}(r_{1,2},\phi)$ does not depend on N. Actually, it reproduces the ground-state energy density in the thermodynamic limit $N \to \infty$ (see Ref. [50] and Fig. 3 in this paper).

Following the interpretation of the variational parameters recently introduced in Ref. [27] for the use in molecular bending problems, the unitless parameters r_1 and r_2 are proportional to physical bending angles and can be both positive and negative. For bent ($r_j \neq 0$) planar configurations there are four possible sign combinations, two for the *cis* case ($r_1r_2 > 0$) and two for the *trans* case ($r_1r_2 < 0$). In the nonplanar case the dihedral angle ϕ is taken as $0 \leqslant \phi \leqslant \pi/2$. Having this in mind, the phase diagram in Ref. [21] has to be reinterpreted because the η_2 parameter in Eq. (2) is limited to negative values in order to get a physically sound spectrum once the Hamiltonian is diagonalized. However, in Ref. [21] only positive r_j values were considered, and thus the right half of the phase diagram (positive η_2 values) is equivalent to what is obtained with $r_1r_2 < 0$ for negative η_2 values. Henceforward we have reinterpreted the results in Ref. [21] with this in mind.

Since $\mathcal{E}_{\xi,\eta_{1,2}}(r_{1,2},\phi)$ is symmetric under the interchange $r_1 \leftrightarrow r_2$ (we are dealing with *ABBA* molecules), the equilibrium configuration values will be located at $|r_{e,1}| = |r_{e,2}| = r_e$. We shall focus on the *cis* configuration ($r_1 = r_2 = r$) and consider the energy surface $\mathcal{E}_{\xi,\eta_{1,2}}(r,\phi) \equiv \mathcal{E}_{\xi,\eta_{1,2}}(r_{1,2} = r,\phi)$ as a function of two variational parameters (r,ϕ) only (the *trans* configuration follows similar steps). Minimizing the energy functional (by solving the coupled set of nonlinear equations $\partial\mathcal{E}_{\xi,\eta_{1,2}}(r,\phi)/\partial r = 0$ and $\partial\mathcal{E}_{\xi,\eta_{1,2}}(r,\phi)/\partial\phi = 0$), one can obtain the equilibrium variational (order) parameters as a function of the control parameters: $r = r_e(\xi,\eta_{1,2})$ and $\phi = \phi_e(\xi,\eta_{1,2})$. A complete phase diagram for $\eta_1 = 0$ and $\eta_1 = 1$ was given in Ref. [21], taking into account the considerations stated above. Here we shall restrict ourselves to two trajectories in the $\eta_1 = 1$ phase diagram, denoted as *vertical* ($\eta_2 = -0.5$ and $0 \leqslant \xi \leqslant 1$) and *horizontal* ($\xi = 0.5$ and $-1 \leqslant \eta_2 \leqslant 0$) *cuts* (see also [50]). The system phase diagram as a function of the control

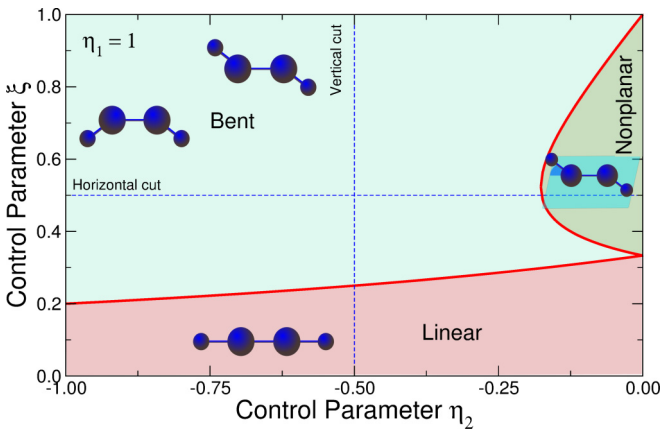

FIG. 1. (Color online) Phase diagram of the coupled 2DVM Hamiltonian (2) as a function of the ξ and η_2 control parameters for $\eta_1 = 1$, showing the three different geometric phases (associated with linear, planar bent, and nonplanar bent molecular configurations). The defined vertical and horizontal cuts in the phase diagram are plotted with thin dashed blue lines. Schematic drawings of symmetric *ABBA* tetratomic molecular species for each case have also been depicted.

parameters ξ and η_2 (for $\eta_1 = 1$) and the aforementioned cuts are depicted in Fig. 1, together with a schematic drawing of the three possible geometric configurations in a tetratomic molecular system: linear, *cis* and *trans* planar bent, and nonplanar bent. The equilibrium radius of the system for the vertical (v) and horizontal (h) cuts is

$$r_v(\xi) = r_e(\xi,\eta_1 = 1,\eta_2 = -1/2) = \begin{cases} 0 & \text{if} \quad \xi \leqslant \xi_c = 1/4, \\ \sqrt{\frac{2}{3}}\sqrt{\frac{4\xi-1}{\xi+1}} & \text{if} \quad \xi > \xi_c, \end{cases}$$
$$r_h(\eta_2) = r_e(\xi = 1/2,\eta_1 = 1,\eta_2) = \begin{cases} \sqrt{\frac{2+4|\eta_2|}{7+4|\eta_2|}} & \text{if} \quad -1 \leqslant \eta_2 < \eta_{2c} = \frac{-1}{8}(\sqrt{41}-5), \\ \sqrt{\frac{2}{5}}\sqrt{1-4\eta_2^2} & \text{if} \quad \frac{-1}{8}(\sqrt{41}-5) \leqslant \eta_2 \leqslant 0, \end{cases} \tag{8}$$

and the equilibrium relative angle is

$$\begin{aligned} \phi_v(\xi) &= \phi_e(\xi,\eta_1 = 1,\eta_2 = -1/2) = 0, \\ \phi_h(\eta_2) &= \phi_e(\xi = 1/2,\eta_1 = 1,\eta_2) \\ &= \begin{cases} 0 & \text{if} \quad -1 \leqslant \eta_2 < \eta_{2c}, \\ \arccos\left(\frac{5\eta_2}{4\eta_2^2-1}\right) & \text{if} \quad \eta_{2c} \leqslant \eta_2 \leqslant 0. \end{cases} \end{aligned} \tag{9}$$

These two quantities can be considered "order parameters" for the shape phase transition.

The mean-field energy density values obtained from the equilibrium values of r and ϕ for the two trajectories in the phase diagram under study are

$$\begin{aligned} E_v(\xi) &= \mathcal{E}_{\xi,1,-1/2}(r_v(\xi),\phi_v(\xi)) \\ &= \begin{cases} \frac{\xi}{2} & \text{if} \quad \xi \leqslant \xi_c, \\ \frac{-2+17\xi-21\xi^2}{2+22\xi} & \text{if} \quad \xi > \xi_c, \end{cases} \\ E_h(\eta_2) &= \mathcal{E}_{1/2,1,\eta_2}(r_h(\eta_2),\phi_h(\eta_2)) \\ &= \begin{cases} \frac{7-8\eta_2^2}{36+32|\eta_2|} & \text{if} \quad -1 \leqslant \eta_2 < \eta_{2c}, \\ \frac{5-20\eta_2^2}{28-32\eta_2^2} & \text{if} \quad \eta_{2c} \leqslant \eta_2 \leqslant 0. \end{cases} \end{aligned} \tag{10}$$

One can prove that $\partial^2 E_v(\xi)/\partial\xi^2$ and $\partial^2 E_h(\eta_2)/\partial\eta_2^2$ are discontinuous at $\xi = \xi_c$ and $\eta_2 = \eta_{2c}$, respectively, which means that we are dealing with second-order quantum phase transitions.

III. PARITY AND SCHRÖDINGER-CAT STATES

Semiclassical CSs defined in Eq. (5) are a convenient tool to analyze the mean-field limit and the phase diagram of the coupled 2DVM. Nevertheless, the CS (5), as will be shown in the next section, does not account for entanglement between benders. This is because it is defined as a direct product. A way to incorporate entanglement into the direct product (5) is through the intrinsic parity symmetry present in the Hamiltonian (2). This has already been done for a single bender in the 2DVM [4,51]. In fact, we have already mentioned that the parity operator $\hat{\Pi} = e^{i\pi\hat{n}}$ commutes with $\hat{H}$, and thus both operators can be jointly diagonalized. The ground state must be of even parity, and it is easy to see that

$$\hat{\Pi}|r_1,\theta_1;r_2,\theta_2\rangle = |-r_1,\theta_1;-r_2,\theta_2\rangle, \tag{11}$$

so that the projection of the CS (5) onto even and odd parities gives as a result

$$\begin{aligned} |r_1,\theta_1;r_2,\theta_2;\pm\rangle &\equiv \frac{(1\pm\hat{\Pi})|r_1,\theta_1;r_2,\theta_2\rangle}{\mathcal{N}_\pm(r_1,r_2)} \\ &= \frac{|r_1,\theta_1;r_2,\theta_2\rangle \pm |-r_1,\theta_1;-r_2,\theta_2\rangle}{\mathcal{N}_\pm(r_1,r_2)}, \end{aligned} \tag{12}$$

where $\mathcal{N}_\pm(r_1,r_2) = \sqrt{2}(1 \pm \langle -r_1,\theta_1;-r_2,\theta_2|r_1,\theta_1;r_2,\theta_2\rangle)^{1/2}$ is a normalization constant, with

$$\langle -r_1,\theta_1;-r_2,\theta_2|r_1,\theta_1;r_2,\theta_2\rangle = \prod_{j=1}^{2}\left(\frac{1-r_j^2}{1+r_j^2}\right)^{N_j}. \tag{13}$$

Note that the overlap (13) is negligible in the large-N (thermodynamic) limit for any r_j; therefore, in this limit, the states (12) are a superposition of two nonoverlapping (distinguishable) quasiclassical (coherent) wave packets (see [47,48] and [52–54] for a similar behavior in the Dicke model). This justifies the denomination of Schrödinger-cat–like for these states. We only discuss the even case (ground-state ansatz); the odd case would correspond to the first-excited-state ansatz. Expanding (12) in the basis (4), as we did in Eq. (6) for the plain CS, we arrive at the new coefficients:

$$\begin{aligned} &|r_1,\theta_1;r_2,\theta_2;+\rangle \\ &\quad = \sum_{n_1,n_2=0}^{N_1,N_2}\sum_{m_1,m_2=0}^{n_1,n_2} s_{m_1,m_2}^{n_1,n_2}(r_1,\theta_1;r_2,\theta_2)\left|n_1^{n_1-2m_1},n_2^{n_2-2m_2}\right\rangle, \\ &s_{m_1,m_2}^{n_1,n_2}(r_1,\theta_1;r_2,\theta_2) \\ &\quad \equiv \frac{\prod_{j=1}^{2} c_{n_j,m_j}^{(N_j)}(r_j,\theta_j) + \prod_{j=1}^{2} c_{n_j,m_j}^{(N_j)}(-r_j,\theta_j)}{\mathcal{N}_\pm(r_1,r_2)}. \end{aligned} \tag{14}$$

Note that now $s_{m_1,m_2}^{n_1,n_2}(r_1,\theta_1;r_2,\theta_2) = 0$ for odd polyad number $n = n_1 + n_2$.

Again, the variational parameters r_j,θ_j are fixed by minimizing the mean energy per particle in the (even) cat state (12):

$$\mathcal{E}_{\xi,\eta_{1,2}}^{(N,+)}(r_{1,2},\phi) = \frac{\langle r_1,\theta_1;r_2,\theta_2;+|\hat{H}|r_1,\theta_1;r_2,\theta_2;+\rangle}{\varepsilon N}, \tag{15}$$

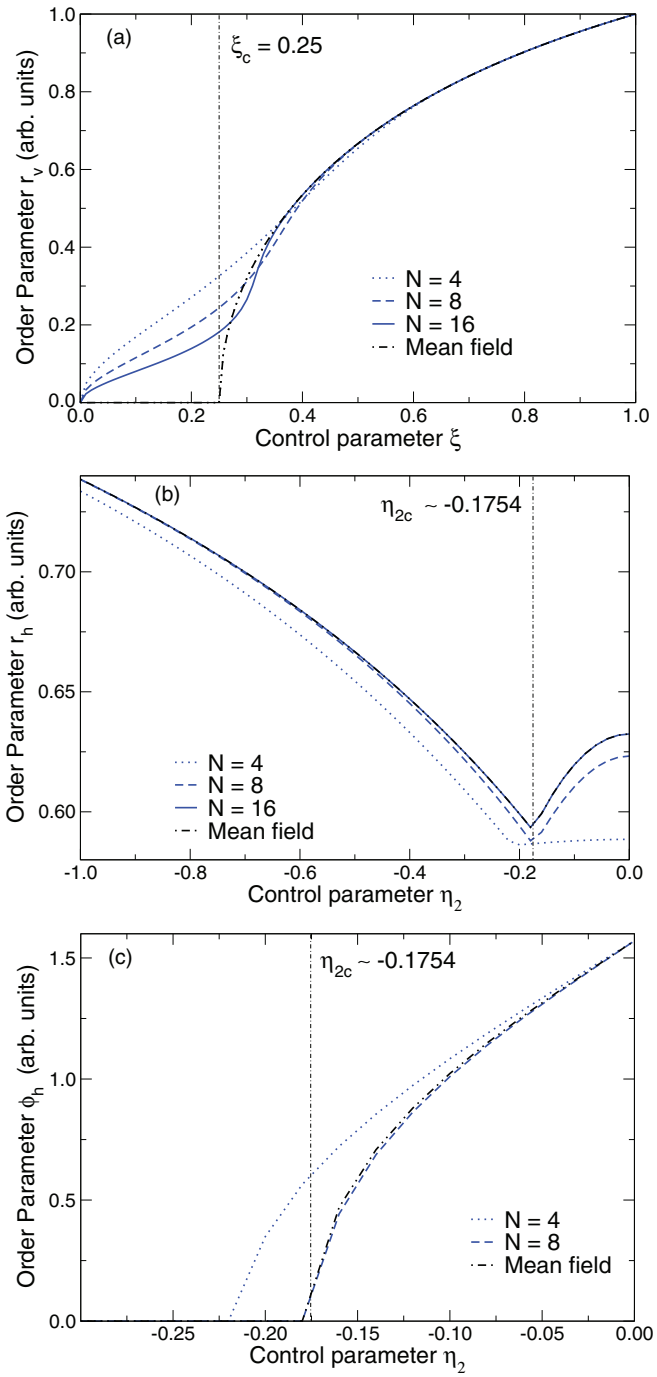

FIG. 2. (Color online) Comparison of the mean-field ($N = \infty$) order parameters with the Schrödinger-cat order parameters for different values of N in the horizontal and vertical cuts in the phase diagram of Fig. 1. (a) $r_v^{(N)}(\xi)$, (b) $r_h^{(N)}(\eta_2)$, and (c) $\phi_h^{(N)}(\eta_2)$. The critical control parameter values $\xi_c = 1/4$ and $\eta_{2c} = \frac{-1}{8}(\sqrt{41} - 5)$ are marked with a vertical thin dot-dashed line in the three cases.

which can be computed in terms of (7) and the off-diagonal matrix elements:

$$\langle r_1,\theta_1;r_2,\theta_2|\hat{n}_j|-r_1,\theta_1;-r_2,\theta_2;\rangle = -N_j\frac{r_j^2}{1-r_j^2}\prod_{k=1}^{2}\left(\frac{1-r_k^2}{1+r_k^2}\right)^{N_k}, \tag{16}$$

$$\langle r_1,\theta_1;r_2,\theta_2|\hat{Q}_1\hat{Q}_2|-r_1,\theta_1;-r_2,\theta_2;\rangle = \cos(2\phi)\prod_{k=1}^{2}N_k\frac{r_k^2}{1-r_k^2}\left(\frac{1-r_k^2}{1+r_k^2}\right)^{N_k}, \tag{17}$$

$$\langle r_1,\theta_1;r_2,\theta_2|\hat{W}_j^2|-r_1,\theta_1;-r_2,\theta_2;\rangle = 2N_j\prod_{k=1}^{2}\left(\frac{1-r_k^2}{1+r_k^2}\right)^{N_k}, \tag{18}$$

$$\langle r_1,\theta_1;r_2,\theta_2|\hat{W}_1\hat{W}_2|-r_1,\theta_1;-r_2,\theta_2;\rangle = 0. \tag{19}$$

Contrary to $\mathcal{E}_{\xi,\eta_{1,2}}(r_{1,2},\phi)$ in Eq. (7), the new energy density $\mathcal{E}^{(N,+)}_{\xi,\eta_{1,2}}(r_{1,2},\phi)$ depends on N. Since $\mathcal{E}^{(N,+)}_{\xi,\eta_{1,2}}(r_{1,2},\phi)$ is also symmetric under the interchange $r_1 \leftrightarrow r_2$, the absolute value of the equilibrium radius coincide, $|r_{e,1}| = |r_{e,2}| = r_e$. For the *cis* configuration, the energy surface $\mathcal{E}^{(N,+)}_{\xi,\eta_{1,2}}(r,\phi) \equiv \mathcal{E}^{(N,+)}_{\xi,\eta_{1,2}}(r_{1,2} = r,\phi)$ is again a function of two variational parameters (r,ϕ).

The minimization of the cat energy functional $\mathcal{E}^{(N,+)}_{\xi,\eta_{1,2}}(r,\phi)$ has to be done numerically in this case. Contrary to the mean-field case, the equilibrium variational (order) parameters $r = r_e^{(N)}(\xi,\eta_{1,2})$ and $\phi = \phi_e^{(N)}(\xi,\eta_{1,2})$ now depend on N and provide finite-N approximations to the mean-field parameters r_e and ϕ_e in Eqs. (8) and (9). A comparison between the cat and CS order parameters for different values of N is depicted in Fig. 2. We denote by $E^{(N)}_{\rm cat}(\xi,\eta_{1,2}) = \mathcal{E}^{(N,+)}_{\xi,\eta_{1,2}}(r_e^{(N)}(\xi,\eta_{1,2}),\phi_e^{(N)}(\xi,\eta_{1,2}))$ the minimum mean energy of the cat state. In Fig. 3 we compare the ground-state energy per particle for the mean-field [Eq. (10)], numeric, and cat cases for different values of N. We realize that the cat energy actually provides a better approximation to the exact (numerical) energy density than the CS or mean-field energy (7) for finite N. Like the exact energy, the cat energy density (15) also tends to the mean-field energy density (7) in the thermodynamic limit $N \to \infty$ [at which the overlap (13) is zero]. Actually, the convergence of the cat energy density to the mean-field energy density is faster than for the numeric case. The biggest difference between the exact and variational energies is located around the critical points, where the ground-state structure deviates from the coherent and cat structures, as expected. To better appreciate this fact, we also represent in Fig. 4 the departure (difference) of the even-cat and mean-field results with the exact (numeric) ground-state energy as a function of the control parameter.

The improvement in the results for these quantities obtained with the newly derived cat states is not their most important characteristic. In fact, beyond mean-field corrections for finite N values can be obtained in a systematic way using an expansion in powers of N [49]. However, as we show in the next section, considering parity in the definition of the cat states allows them to reproduce the exact entanglement properties of the coupled 2DVM model.

IV. ENTANGLEMENT IN COUPLED MOLECULAR BENDERS

In this section we quantify the entanglement between the two coupled benders and the rovibrational entanglement through the vertical and horizontal cuts in the phase diagram in Fig. 1. Let us denote the normalized ground-state wave

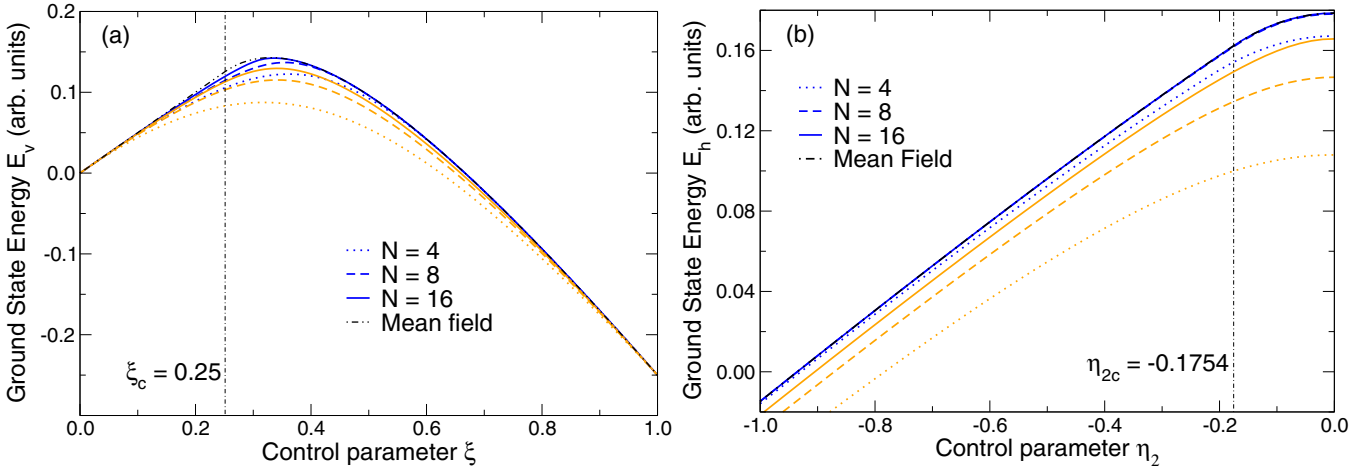

FIG. 3. (Color online) Ground-state energy per particle for the (a) vertical (E_v, $\eta_1 = 1, \eta_2 = -0.5 \Rightarrow \xi_c = 1/4$) and (b) horizontal [$E_h$, $\eta_1 = 1, \xi = 0.5 \Rightarrow \eta_{2c} = \frac{-1}{8}(\sqrt{41} - 5)$] cuts in the phase diagram (see Fig. 1). Mean-field results are depicted with a dot-dashed black line, even-cat results for $N = 4,8,16$ are depicted with dotted, dashed, and solid blue (dark gray) lines, and exact (numeric) results for the same N values are depicted with dotted, dashed, and solid orange (light gray) lines. The critical values of the control parameters are marked with a vertical thin dot-dashed line in both panels.

function by

$$|\psi_{\xi,\eta_1,\eta_2}\rangle = \sum_{n_1,n_2=0}^{N/2} \sum_{m_1,m_2=0}^{n_1,n_2} c_{m_1,m_2}^{n_1,n_2}(\xi,\eta_1,\eta_2)\left|n_1^{\ell_1}; n_2^{\ell_2}\right\rangle,$$
$$\ell_{1,2} = n_{1,2} - 2m_{1,2}, \tag{20}$$

where the c coefficients are obtained by a numerical diagonalization of the Hamiltonian (2).

A. Entanglement between benders

Let us first consider the two coupled molecular benders $j = 1,2$ as a bipartite system, with density matrix $\rho(\xi,\eta_1,\eta_2) = |\psi_{\xi,\eta_1,\eta_2}\rangle\langle\psi_{\xi,\eta_1,\eta_2}|$. Taking, for example, the partial trace with respect to the second bender, we obtain the reduced density matrix (RDM) $\rho_1 = \mathrm{Tr}_2(\rho)$ for the first bender, with matrix elements

$$\rho_1{}_{m_1,m_1'}^{n_1,n_1'}(\xi,\eta_1,\eta_2) = \sum_{n_2=0}^{N/2} \sum_{m_2=0}^{n_2} c_{m_1,m_2}^{n_1,n_2}(\xi,\eta_1,\eta_2)\overline{c_{m_1',m_2}^{n_1',n_2}(\xi,\eta_1,\eta_2)}. \tag{21}$$

The purity of ρ_1 is then given by

$$\mathrm{Tr}\left[\rho_1^2(\xi,\eta_1,\eta_2)\right] = \sum_{n_1,n_1'=0}^{N/2} \sum_{m_1,m_1'=0}^{n_1,n_1'} \rho_1{}_{m_1,m_1'}^{n_1,n_1'}(\xi,\eta_1,\eta_2)\rho_1{}_{m_1',m_1}^{n_1',n_1}(\xi,\eta_1,\eta_2). \tag{22}$$

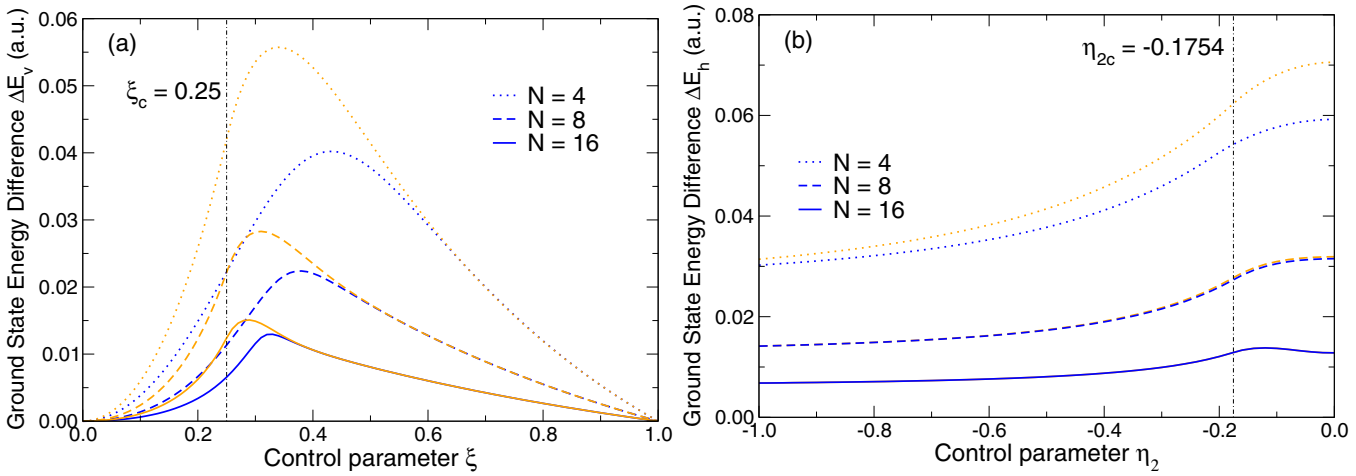

FIG. 4. (Color online) Departure (difference) of the even-cat [blue (dark gray) lines] and mean-field [orange (light gray) lines] results from the exact (numeric) results for the ground-state energy density in the (a) vertical (ΔE_v, $\eta_1 = 1, \eta_2 = -0.5 \Rightarrow \xi_c = 1/4$) and (b) horizontal [$\Delta E_h$, $\eta_1 = 1, \xi = 0.5 \Rightarrow \eta_{2c} = \frac{-1}{8}(\sqrt{41} - 5)$] cuts in the phase diagram (see Fig. 1). The difference between mean-field results and exact results for $N = 4,8,16$ are depicted with dotted, dashed, and solid orange (light gray) lines. The difference between even-cat and exact results for the same N values are depicted with dotted, dashed, and solid blue (dark gray) lines. The critical values of the control parameters are marked with a vertical thin dot-dashed line in both panels.

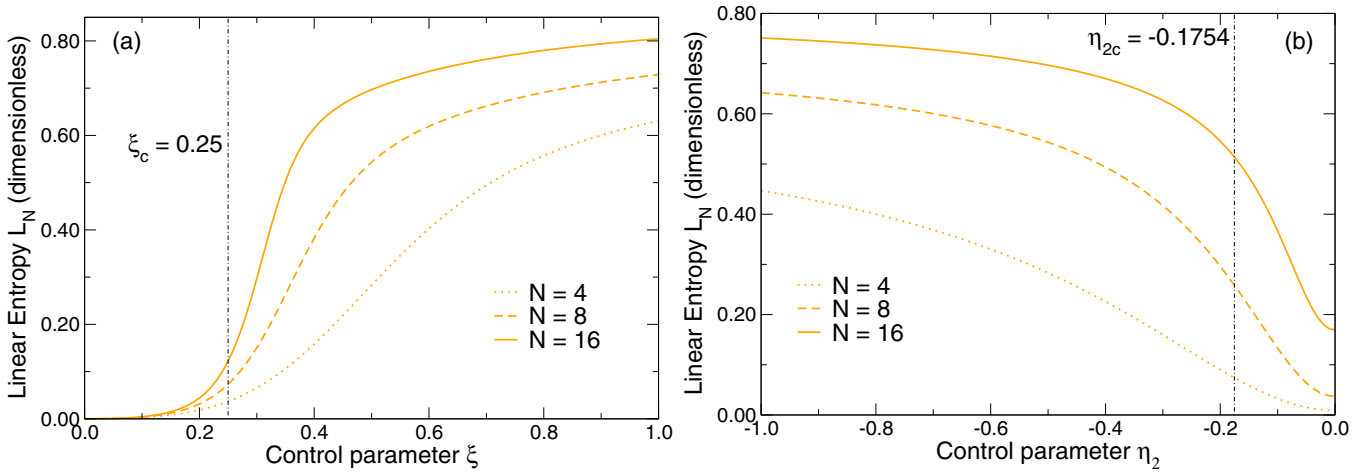

FIG. 5. (Color online) Exact (numeric) linear entropy $L_N(\xi,\eta_1,\eta_2)$ for $N = 4,8,16$ as a function of the control parameters (a) ξ (vertical cut; $\eta_1 = 1, \eta_2 = -1/2 \Rightarrow \xi_c = 1/4$) and (b) η_2 [horizontal cut; $\eta_1 = 1, \xi = 1/2 \Rightarrow \eta_{2c} = \frac{-1}{8}(\sqrt{41} - 5)$; see Fig. 1]. The critical values of the control parameters are marked with a vertical thin dot-dashed line in both panels.

We shall use the linear entropy ("impurity")

$$L_N(\xi,\eta_1,\eta_2) = 1 - \mathrm{Tr}\left[\rho_1^2(\xi,\eta_1,\eta_2)\right] \tag{23}$$

as a measure of the entanglement between the two benders. The exact (numerical) results for the ground-state linear entropy are depicted in Fig. 5 for the two particular cuts mentioned above: (1) phase transition from linear to bent (*cis*) as a function of ξ (critical point at $\xi_c = 1/4$) for $\eta_1 = 1$ and $\eta_2 = -1/2$ and (2) phase transition from *cis* to nonplanar [critical point at $\eta_{2c} = \frac{-1}{8}(\sqrt{41} - 5)$]. The transition from *trans* to nonplanar gives similar results. We see that, in the first case, the impurity L_N grows with ξ and N in passing from the linear to bent-*cis* phase, and this growth becomes sharper as N increases. In the second case, the two benders are more entangled in the *cis* (and *trans*) phase than in the nonplanar configuration.

As already mentioned, the coherent state (5), being a direct product, does not capture the entanglement between the two benders. Let us see how the projection (12) of (5) on good parity (i.e., the cat state) does capture the qualitative behavior of the linear entropy across the phase transition. Indeed, plugging the cat coefficients $c^{n_1,n_2}_{m_1,m_2}(\xi,\eta_{1,2}) = s^{n_1,n_2}_{m_1,m_2}(r_e^{(N)},\phi_e^{(N)})$ [given in Eq. (14)] into (21)–(23), we can compute the linear entanglement entropy of the cat state (12). Figure 6 shows the linear entanglement entropy of the cat state for the two cases mentioned above. We see that the cat state captures the growth of entanglement in the bent (*cis* and *trans*) phase, although it does not match the numerical values of Fig. 5.

This means that the adaptation of the variational coherent state to parity (which results in a catlike state) is *necessary* to account for entanglement between benders (at least to capture the exact linear entropy qualitative behavior), but it does not seem to be *sufficient* to reach a good quantitative agreement too. To better fit the exact (numerical) entropy values, further structure should be allowed for the variational state, perhaps in

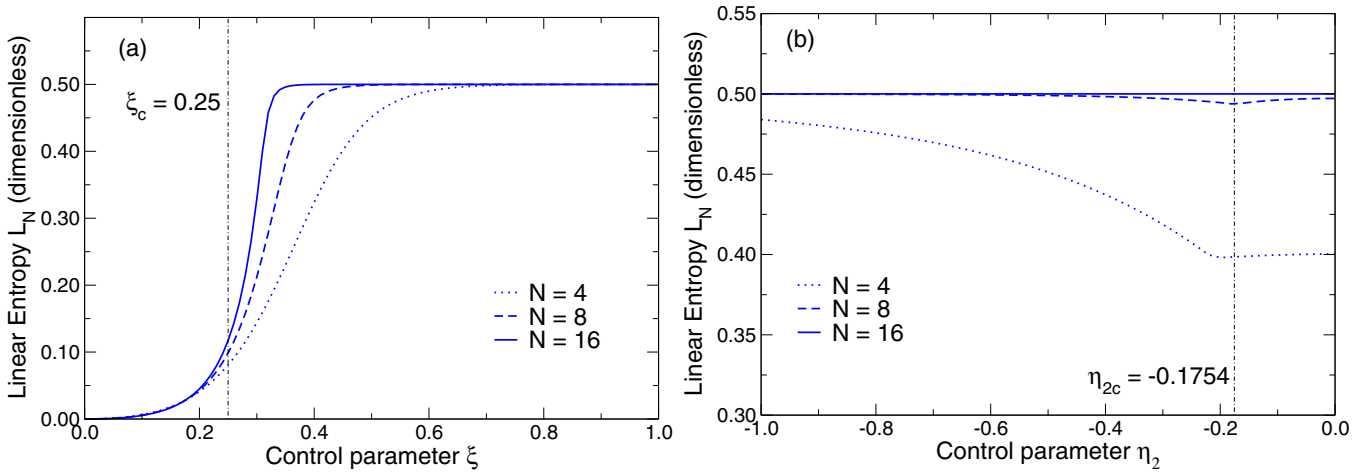

FIG. 6. (Color online) Variational (even-cat) linear entanglement entropy $L_N(\xi,\eta_1,\eta_2)$ for $N = 4,8,16$ as a function of the control parameters (a) ξ (vertical cut; $\eta_1 = 1, \eta_2 = -1/2 \Rightarrow \xi_c = 1/4$) and (b) η_2 [horizontal cut; $\eta_1 = 1, \xi = 1/2 \Rightarrow \eta_{2c} = \frac{-1}{8}(\sqrt{41} - 5)$; see Fig. 1]. The critical values of the control parameters are marked with a vertical thin dot-dashed line in both panels.

the form of extra variational parameters. Anyway, it is always complicated to find variational states which reproduce several exact state properties at the same time, especially for finite-N nonlinear coupled systems like the one at hand.

B. Rovibrational entanglement

Now we shall study a second case of interest, the entanglement between rotational and vibrational degrees of freedom. Let us denote by

$$\psi_{\xi,\eta_{1,2}}(q_1;q_2)=\langle q_1;q_2|\psi_{\xi,\eta_1,\eta_2}\rangle \tag{24}$$

the system wave function in "position" representation $q_j=(q_j^0,\vec{q}_j), j=1,2$, where q_j^0 denote the coordinates for the scalar bosons σ_j (carrying zero angular momentum) and $\vec{q}_j=(q_j^+,q_j^-)$ are the coordinates for the vector bosons $\vec{\tau}_j=(\tau_{+,j},\tau_{-,j})$ representing dipole excitations of the molecule and carrying unit angular momentum (in three-dimensional configurations). The wave function (24) can be expanded in terms of Hermite polynomials $H_k(q)$ by noting that basis (4) comprises wave functions

$$\langle q_1;q_2|n_1^{\ell_1},n_2^{\ell_2}\rangle=\prod_{j=1}^{2}\frac{2^{-N_j/2}\pi^{-3/4}e^{-[(q_j^0)^2+(\vec{q}_j)^2]/2}}{\sqrt{(N_j-n_j)!\left(\frac{n_j+\ell_j}{2}\right)!\left(\frac{n_j-\ell_j}{2}\right)!}}\times H_{N_j-n_j}(q_j^0)H_{\frac{n_j+\ell_j}{2}}(q_j^+)H_{\frac{n_j-\ell_j}{2}}(q_j^-). \tag{25}$$

We consider the bipartite system given by scalar (q^0) and vector [$\vec{q}=(q^+,q^-)$] degrees of freedom. Then, we can compute the reduced density matrix for scalar degrees of freedom (we call it $\rho^{(\mathrm{v})}_{\xi,\eta_{1,2}}$ for the reasons given below) by integrating out the vector degrees of freedom

$$\rho^{(\mathrm{v})}_{\xi,\eta_{1,2}}(q_1^0,q_2^0;q_1'^0,q_2'^0)=\int_{\mathbb{R}^2}\int_{\mathbb{R}^2}d\vec{q}_1d\vec{q}_2\,\psi_{\xi,\eta_{1,2}}(q_1^0,\vec{q}_1;q_2^0,\vec{q}_2)\times\bar{\psi}_{\xi,\eta_{1,2}}(q_1'^0,\vec{q}_1;q_2'^0,\vec{q}_2). \tag{26}$$

The purity of $\rho^{(\mathrm{v})}_{\xi,\eta_{1,2}}$ is given by

$$\mathrm{Tr}\left(\rho^{(\mathrm{v})}_{\xi,\eta_{1,2}}\right)^2=\int_{\mathbb{R}}\int_{\mathbb{R}}\int_{\mathbb{R}}\int_{\mathbb{R}}dq_1^0dq_2^0dq_1'^0dq_2'^0\rho^{(v)}_{\xi,\eta_{1,2}}\times(q_1^0,q_2^0;q_1'^0,q_2'^0)\rho^{(v)}_{\xi,\eta_{1,2}}(q_1'^0;q_2'^0;q_1^0,q_2^0)=\sum_{n_1=0}^{N/2}\sum_{n_2=0}^{N/2}\left(\sum_{m_1=0}^{n_1}\sum_{m_2=0}^{n_2}\left|c^{n_1,n_2}_{m_1,m_2}(\xi,\eta_1,\eta_2)\right|^2\right)^2, \tag{27}$$

where we have used the orthogonality properties of the basis functions (25) and the coefficients of the expansion (20). Integrating out vector degrees of freedom, as in Eq. (26), is equivalent to taking the partial trace with respect to angular momentum (rotational) quantum numbers $\ell_j=n_j-2m_j, m_j=0,\ldots,n_j$ ($j=1,2$) for fixed vibrational quantum numbers $n_j, j=1,2$. Indeed, the reduced density matrix $\rho^{(\mathrm{v})}_{\xi,\eta_{1,2}}$ elements in the discrete basis (4) can be written as

$$\left(\rho^{(\mathrm{v})}_{\xi,\eta_{1,2}}\right)^{n_2,n_2'}_{n_1,n_1'}=\sum_{m_1=0}^{n_1}\sum_{m_2=0}^{n_2}\left|c^{n_1,n_2}_{m_1,m_2}(\xi,\eta_1,\eta_2)\right|^2\delta_{n_1,n_1'}\delta_{n_2,n_2'}, \tag{28}$$

whose purity is precisely (27). This justifies our proposal of $\rho^{(\mathrm{v})}_{\xi,\eta_{1,2}}$ as the reduced density matrix for vibrational (v) modes.

We shall denote the rovibrational linear entanglement entropy by

$$L_N^{(\mathrm{v})}(\xi,\eta_1,\eta_2)=1-\mathrm{Tr}\left(\rho^{(\mathrm{v})}_{\xi,\eta_{1,2}}\right)^2 \tag{29}$$

to distinguish it from (23). Figure 7 gives a comparison between exact (numeric) and variational (cat) rovibrational linear entanglement entropies for the linear-*cis* and *cis*-nonplanar transitions. We observe good agreement between numeric and variational results, mainly for rigid molecules. The entanglement entropy captures the QPT, especially the one from linear to *cis* (and *trans*), that causes a sudden growth at the critical point ξ_c, which sharpens as the N value increases.

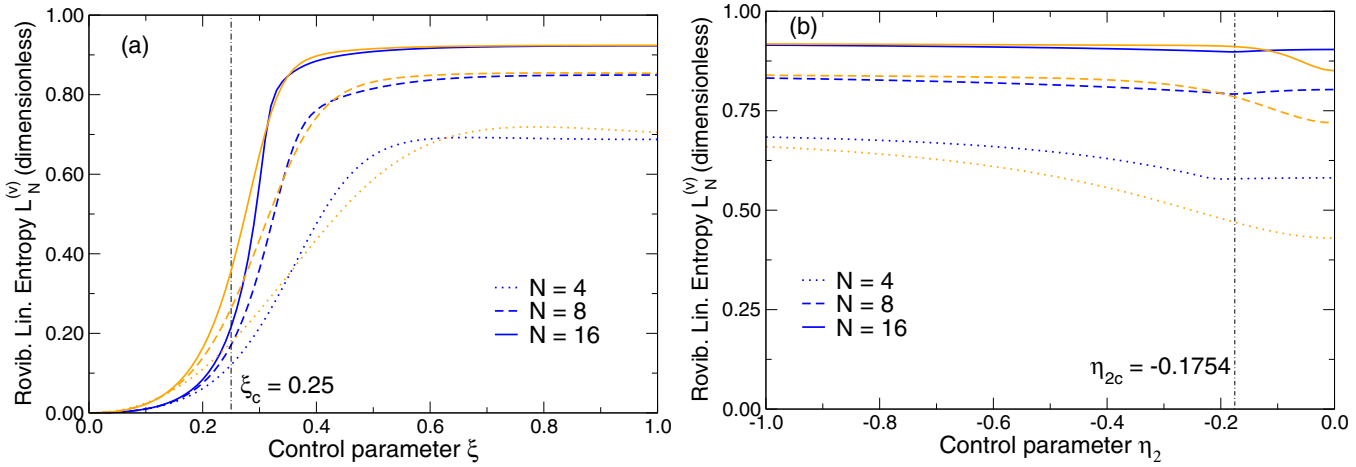

FIG. 7. (Color online) Rovibrational linear entropy $L_N^{(v)}(\xi,\eta_1,\eta_2)$ for the exact [numerical, orange (light gray) lines] and even-cat [variational, blue (dark gray) lines] cases. Results are depicted for $N=4,8,16$ as a function of (a) ξ (vertical cut; $\eta_1=1,\eta_2=-1/2\Rightarrow\xi_c=1/4$) and (b) η_2 [horizontal cut; $\eta_1=1,\xi=1/2\Rightarrow\eta_{2c}=\frac{-1}{8}(\sqrt{41}-5)$; see Fig. 1]. The critical values of the control parameters are marked with a vertical thin dot-dashed line in both panels.

The asymptotic behavior for the rovibrational linear entanglement entropy for $\eta_1 = 1, \eta_2 = -1/2, \xi = 1$ and $\eta_1 = 1, \eta_2 = -1, \xi = 1/2$ scales with N according to

$$L_N^{(\mathrm{v})} \simeq 1 - \frac{4}{\pi N}, \tag{30}$$

as can be directly checked in Fig. 7 for $N = 4, 8$, and 16.

V. CONCLUSIONS

We have studied quantum ground-state correlations of coupled molecular benders across several possible geometric configurations: from linear to bent (*cis* or *trans*) and from bent (*cis* or *trans*) to nonplanar. In particular, we have computed quantum correlations between benders and quantum correlations between rotational and vibrational degrees of freedom using the linear entanglement entropy (impurity) to quantify them. A variational approach in terms of coherent states has been used for a semiclassical (mean-field) study and to complement numerical calculations. We realize that a projection of coherent states on good parity (which results in a Schrödinger-cat–like state) is necessary to reproduce numerical results of entanglement. For bender-bender entanglement, variational (even-cat) results qualitatively reproduce numerical results, both displaying a sudden change of impurity at the critical points. The results indicate that benders are correlated in bent and nonplanar configurations but not in the linear phase. For rovibrational entanglement, variational results not only capture the qualitative behavior but also show a quite good quantitative agreement with numerical calculations. The purity results show that rotational and vibrational degrees of freedom are entangled in the bent (*cis* or *trans*) and nonlinear phases. In the bent phase, purity scales with N as $\frac{4}{\pi N}$, which means that rovibrational entanglement is not maximal since minimal rovibrational purity would be $\frac{1}{(N+1)^2}$. In the thermodynamical $N \to \infty$ limit, rovibrational linear entropy (purity) attains its maximum (minimum).

The question of how to use this entanglement between molecular benders for potential quantum information processes remains. Emission, absorption, and scattering of phonons and rotons have been extensively studied in superfluid helium. Perhaps quantum correlations between rotational and vibrational degrees of freedom in coupled molecular benders could also provide feasible quantum (communication and computation) protocols. For the time being, we think that it is interesting to show the existence of quantum correlations in these vibron models.

ACKNOWLEDGMENTS

The authors thank J. M. Arias and F. Iachello for discussions and valuable comments. Work was partially supported by the Spanish MINECO under projects FIS2011-29813-C02-01 and FIS2011-28738-C02-02 and by the University of Granada under project PP2012-PI04.

[1] N. Lambert, C. Emary, and T. Brandes, Phys. Rev. Lett. **92**, 073602 (2004).
[2] N. Lambert, C. Emary, and T. Brandes, Phys. Rev. A **71**, 053804 (2005).
[3] C. Pérez-Campos, J. R. González-Alonso, O. Castaños, and R. López-Peña, Ann. Phys. (NY) **325**, 325 (2010).
[4] M. Calixto, E. Romera, and R. del Real, J. Phys. A **45**, 365301 (2012).
[5] F. Iachello, Chem. Phys. Lett. **78**, 581 (1981).
[6] F. Iachello and R. D. Levine, *Algebraic Theory of Molecules* (Oxford University Press, Oxford, 1995).
[7] F. Iachello and A. Arima, *The Interacting Boson Model* (Cambridge University Press, Cambridge, 1987).
[8] F. Iachello and S. Oss, J. Chem. Phys. **104**, 6956 (1996).
[9] F. Iachello, F. Pérez-Bernal, and P. H. Vaccaro, Chem. Phys. Lett. **375**, 309 (2003).
[10] F. Pérez-Bernal, L. F. Santos, P. H. Vaccaro, and F. Iachello, Chem. Phys. Lett. **414**, 398 (2005).
[11] F. Pérez-Bernal and F. Iachello, Phys. Rev. A **77**, 032115 (2008).
[12] D. Larese and F. Iachello, J. Mol. Struct. **1006**, 611 (2011).
[13] D. Larese, F. Pérez-Bernal, and F. Iachello, J. Mol. Struct. **1051**, 310 (2013).
[14] R. Gilmore, J. Math. Phys. **20**, 891 (1979).
[15] P. Cejnar and J. Jolie, Prog. Part. Nucl. Phys. **62**, 210 (2009).
[16] R. F. Casten, Prog. Part. Nucl. Phys. **62**, 183 (2009).
[17] P. Cejnar, J. Jolie, and R. F. Casten, Rev. Mod. Phys. **82**, 2155 (2010).
[18] S. Oss and M. Abbouti Temsamani, J. Chem. Phys. **108**, 1773 (1998).
[19] F. Iachello and F. Pérez-Bernal, J. Phys. Chem. A **113**, 13273 (2009).
[20] F. Iachello and F. Pérez-Bernal, Mol. Phys. **106**, 223 (2008).
[21] F. Pérez-Bernal and L. Fortunato, Phys. Lett. A **376**, 236 (2012).
[22] J. M. Arias, J. E. García-Ramos, and J. Dukelsky, Phys. Rev. Lett. **93**, 212501 (2004).
[23] M. A. Caprio and F. Iachello, Phys. Rev. Lett. **93**, 242502 (2004).
[24] M. A. Caprio and F. Iachello, Ann. Phys. (NY) **318**, 454 (2005).
[25] M. Abbouti Temsamani, J.-M. Champion, and S. Oss, J. Chem. Phys. **110**, 2893 (1999).
[26] J. M. Champion, M. A. Temsamani, and S. Oss, Chem. Phys. Lett. **308**, 274 (1999).
[27] D. Larese, M. Caprio, F. Pérez-Bernal, and F. Iachello, J. Chem. Phys. **140**, 014304 (2014).
[28] G. Strey and I. M. Mills, J. Mol. Spectrosc. **59**, 103 (1976).
[29] V. Tyng and M. E. Kellman, J. Phys. Chem. B **110**, 18859 (2006).
[30] A. J. Merer *et al.*, J. Chem. Phys. **129**, 054304 (2008).
[31] V. Tyng and M. E. Kellman, J. Chem. Phys. **130**, 144311 (2009).
[32] J. H. Baraban, J. F. Stanton, A. J. Merer, and R. W. Field, Mol. Phys. **110**, 2725 (2012).
[33] V. Tyng and M. E. Kellman, J. Chem. Phys. **131**, 244111 (2009).
[34] V. Tyng and M. E. Kellman, J. Phys. Chem. A **114**, 9825 (2010).
[35] A. Perelomov, *Generalized Coherent States and Their Applications* (Springer, Berlin, 1986).
[36] J. R. Klauder and B. S. Skagerstam, *Coherent States: Applications in Physics and Mathematical Physics* (World Scientific, Singapore, 1985).

[37] S. T. Ali, J.-P. Antoine, and J. P. Gazeau, *Coherent States, Wavelets and Their Generalizations* (Springer, New York, 2000).
[38] A. Vourdas, J. Phys. A **39**, R65 (2006).
[39] B. C. Sanders, J. Phys. A **45**, 244002 (2012).
[40] J. N. Ginocchio and M. W. Kirson, Phys. Rev. Lett. **44**, 1744 (1980).
[41] A. Bohr and B. R. Mottelson, Phys. Scr. **22**, 468 (1980).
[42] A. E. L. Dieperink, O. Scholten, and F. Iachello, Phys. Rev. Lett. **44**, 1747 (1980).
[43] O. S. van Roosmalen, Ph.D. thesis, University of Groningen, 1982.
[44] O. S. van Roosmalen, R. D. Levine, and A. E. L. Dieperink, Chem. Phys. Lett. **101**, 512 (1983).
[45] A. Leviatan and M. W. Kirson, Ann. Phys. (NY) **188**, 142 (1988).
[46] R. F. Bishop and A. Vourdas, Phys. Rev. A **50**, 4488 (1994).
[47] O. Castaños, E. Nahmad-Achar, R. López-Peña, and J. G. Hirsch, Phys. Rev. A **83**, 051601 (2011).
[48] O. Castaños, E. Nahmad-Achar, R. López-Peña, and J. G. Hirsch, Phys. Rev. A **84**, 013819 (2011).
[49] P. Pérez-Fernández, J. M. Arias, J. E. García-Ramos, and F. Pérez-Bernal, Phys. Rev. A **83**, 062125 (2011).
[50] F. Pérez-Bernal and L. Fortunato, in *Beauty in Physics: Theory and Experiment: In Honor of Francesco Iachello on the Occasion of His 70th Birthday*, edited by R. Bijker, AIP Conf. Proc. No. 1488 (AIP, New York, 2012), pp. 350–357.
[51] M. Calixto, R. del Real, and E. Romera, Phys. Rev. A **86**, 032508 (2012).
[52] E. Romera, M. Calixto, and A. Nagy, Europhys. Lett. **97**, 20011 (2012).
[53] M. Calixto, A. Nagy, I. Paradela, and E. Romera, Phys. Rev. A **85**, 053813 (2012).
[54] E. Romera, R. del Real, and M. Calixto, Phys. Rev. A **85**, 053831 (2012).